

Supplementary Information

CO₂ reduction on pure Cu produces only H₂ after subsurface O is depleted: theory and experiment

Guiji Liu^{1,2,#}, Michelle Lee^{1,2,4,#}, Soonho Kwon^{3,#}, Guosong Zeng², Johanna Eichhorn^{1,2,6}, Aya K. Buckley^{1,2,5}, F. Dean Toste,^{1,5} William A. Goddard III^{3,*}, and Francesca M. Toma^{1,2,*}.

¹Joint Center for Artificial Photosynthesis, Lawrence Berkeley National Laboratory, 1 Cyclotron Road, Berkeley, CA 94720, USA.

²Chemical Sciences Division, Lawrence Berkeley National Laboratory, 1 Cyclotron Road, Berkeley, CA 94720, USA.

³Materials Simulation Center and Joint Center for Artificial Photosynthesis, California Institute of Technology, Pasadena, CA 91125, USA.

⁴Department of Chemistry and Chemical Biology, Cornell University, Ithaca, NY 14853, USA.

⁵Department of Chemistry, University of California, Berkeley, CA 94720, USA.

⁶Walter Schottky Institut and Physik Department, Technische Universität München, Am Coulombwall 4, 85748 Garching, Germany

*Correspondence to: wag@caltech.edu; fntoma@lbl.gov

#G.L, M.L, and S.K contributed equally to this work.

This PDF file includes:

Supplementary text

Figures S1 to S23

Tables S1 to S6

Supplementary references

Supporting Information Text

Materials

All chemicals were obtained from commercial suppliers and used without further purification, unless otherwise noted. Copper sulfate pentahydrate (98%), lactic acid (85%), sodium hydroxide (98%) were purchased from Sigma Aldrich. Nitric acid (70%) and high purity potassium carbonate (99.995%) were purchased from Sigma Aldrich. Hydrochloric acid (36.5 – 38%) was purchased from VWR. Isopropyl alcohol (100%) was purchased from KMG electronic chemicals. Water used for all of the synthesis and electrochemical experiments (MilliQ water) was from a Milli-Q Water Purification System (resistivity of 18.2 M Ω -cm, Millipore). Selemion AMV anion-exchange membrane was purchased from AGC Engineering Co., LTD. Carbon dioxide (99.995%) and nitrogen (99.999%) were obtained from Praxair.

Materials characterizations

Scanning electron microscopy (SEM) images were obtained on a scanning electron microscope (Quanta FEG 250, 148 FEI). Grazing incidence X-ray diffraction (GIXRD) was conducted by an X-ray diffractometer (SmartLab, 141Rigaku) using Cu K α radiation at 0.5° grazing angle. Transmission Electron Microscopy (TEM) measurements were conducted on a FEI F20 UT Tecnai microscope at the National Center for Electron Microscopy (NCEM) using a single tilt holder and an accelerating voltage of 200 kV. Quasi in-situ electrochemical atomic force microscopy (EC-AFM) was carried out using a commercial AFM system (Bruker Dimension ICON). PeakForce mode was used to acquire the surface morphology using a Bruker AFM probe with spring constant of 0.7 N/m (Bruker Scanasyt – Fluid+). A planar Cu or Cu₂O samples was compressed within an electrochemical cell as the working electrode and two platinum wires were used as counter

electrode and reference electrode. The pristine surface was measured first, then the probe was retracted and a constant bias with $-0.8 V_{\text{RHE}}$ was applied to the sample. This potential allows for similar operating potential in the CO_2RR measurements ($-1.0 V_{\text{RHE}}$), while minimizing the adverse impact of bubble formation during AFM measurements. Surface morphology was then collected by AFM under open circuit conditions. This procedure was repeated over a period of 5 min in the same sample region to examine the topography and surface roughness (R_a). In-situ Raman spectroscopy was carried out on a confocal Raman microscope (LabRam HR, Horiba Jobin Yvon) in 0.1 M K_2CO_3 (CO_2 saturated) at $-1.0 V_{\text{RHE}}$, using a wavelength of 532 nm. The surface chemical composition was obtained by X-ray photoelectron spectroscopy (XPS) using a Kratos Axis Ultra DLD system at a takeoff angle of 0° relative to the surface normal. A monochromatic Al $K\alpha$ source with emission energy of 1486.6 eV was used to excite the core level electrons of the material. C 1s, Cu 2p, and O 1s core levels were collected, with pass energy of 20 eV, step size of 0.05 eV, and 10 sweeps each to obtain a good signal to noise ratio. All the core levels measured in this paper were corrected using the Cu 2p of pure copper at 932.5 eV. The sample was loaded to the chamber within 2 minutes after the EC test was done to minimize the oxidation of the material. Spectral fitting was conducted using CasaXPS analysis software. The angle-resolved X-ray photoelectron spectroscopy (AR-XPS) with the sample bar tilted with 60° was also conducted to obtain more surface information.

Product detection

Electrochemical experiments were conducted in a two-compartment flow cell fabricated from PEEK. A Selemion AMV anion-exchange membrane separated the two chambers. A Pt foil was used as the counter electrode. A Leak-Free Ag/AgCl electrode (LF-1, 1.0 mm outer diameter, Innovative Instruments, Inc.) was used as the reference electrode. The reference electrode was

calibrated against a second reference electrode, which in turn was calibrated in a two-electrode system with H₂ bubbled over a Pt wire as the counter electrode and a 1M H₂SO₄ solution as the electrolyte. The applied potentials were converted from Ag/AgCl scale to the RHE scale via the equation: $E_{\text{RHE}} = E_{\text{Ag/AgCl}} + 0.197 + 0.059 \times \text{pH}$, where the pH used is the bulk pH for the CO₂-saturated electrolyte (6.9). In the electrochemical cell, the prepared 0.1 M potassium carbonate solution was used as electrolyte. The electrolyte was saturated with a continuous flow of 5 sccm CO₂ for a minimum of 15 minutes within the experimental cell setup immediately prior to all electrochemical experiments. One cycle of chronoamperometric (CA) measurement was performed by applying a constant potential for 65 minutes. Electrochemical experiments were carried out using SP-200 potentiostat from BioLogic. Cyclic voltammetry (CV) was then performed and repeated at the end of each run in order to test the stability of material before and after the chronoamperometric measurement. Chronoamperometric measurement was performed for about 65 minutes. Gas products were quantified using gas chromatography (GC), SRI Instruments with multiple gas analyzer #5, through flow mode. Liquid products were quantified after electrochemical measurement using high performance liquid chromatography (HPLC), UltiMate 3000. During the chronoamperometric measurement, gas from the cell was directed through the sampling loop of a gas chromatograph and was analyzed in 15 minutes intervals. For each interval, concentration of gas produced was collected. With total current density measured at the end of experiment and applied potential, faradaic efficiency for each gas for each interval was calculated. These recorded faradaic efficiencies were averaged and reported.

Derivation of grand canonical potential (GCP)

Most previous theoretical studies for electrochemistry have exploited the computational hydrogen electrode (CHE) for the elementary reduction reaction by proton-coupled electron transfer (PCET).

Therefore, most calculations are based solely on the conventional neutral charge calculation with implicit energy correction of potential dependent PCET. This does not capture the information needed to predict the rates from the explicit effect of applied potential, U .

In contrast, we allow the geometry and free energy along the reaction pathway to change as a function of potential. We first calculate the each state including transition state using a range of net charges which corresponds to the potential of interest. We optimize the geometry using VASP with the VASPsol solvation model, then we use the more accurate CANDLE solvation with Poisson-Boltzmann model for ionic screening which are implemented in JDFTx to calculate the applied potential (U) for every structure.

To Legendre transform the canonical free energy (F) into grand canonical free energy (G), we need the accurate description of F as function of the number of electron (n). For the canonical free energy, we defined,

$$F(n) = a(n - n_0)^2 + b(n - n_0) + c \quad (1)$$

where n_0 the number of electrons at PZC, n is the number of electrons at the given potential, and the constants, a , b , and c , can be determined directly fitting to free energies from JDFTx single point calculations using fully optimized geometry from VASP.

The grand canonical free energy is defined as

$$G(n; U) = F(n) - ne(U_{SHE} - U) = a(n - n_0)^2 + b(n - n_0) + c - ne(U_{SHE} - U) \quad (2)$$

where U is the applied potential and U_{SHE} is the electronic energy at the standard hydrogen electrode (SHE). Here, n is the only unknown for obtaining $G(n;U)$ at given U .

Since n must be equilibrated to U , we can get the equilibrium n at U from,

$$\frac{dG(n,U)}{dn} = 0 \quad (3)$$

which leads to,

$$n = -\frac{b-e(U_{SHE}-U)}{2a} + n_0 \quad (4)$$

The final $G(n; U)$ can be obtained by substitute n from eq. (2) into eq. (4).

It is also possible to describe $G(n; U)$ using physical quantities.

$$G(n; U) = \frac{e^2 C_{diff}}{2} (U - U_{PZC})^2 + n_0 eU + F_0 - n_0 \mu_{e,SHE}$$

where C_{diff} is the differential capacitance, $\frac{\partial n}{\partial U} = -\frac{1}{2a}$, and U_{PZC} is the potential of zero charge. We used $\mu_{e,SHE} = 4.66$ V for CANDLE solvation.

Our approach uses the capacitive effect of the heterogeneous system to obtain a continuous description of $G(U)$ for any state without sacrificing efficiency. The capacitive term also reflects the interfacial double layer capacitance from the Poisson-Boltzmann model. Clearly, this term is necessary to describe the energy of a state as a function of net charge precisely since it has a quadratic dependence on the charge.

To compare the GCP and a simple linear fitting of G , we first calculated the grand canonical free energy ($G = F - n \times \mu_e$ where F : Helmholtz energy, n : number of electrons in a system, μ_e : electron chemical potential) of $2CO^*$ state on Cu(111) surface as a reference energy. Then, we made a direct comparison of GCP and the linear fitting method. The energy deviations of GCP (blue) and the linear fit (green) from explicit ($F - n \times \mu_e$, red) calculation at each potential as shown in Figure S1a.

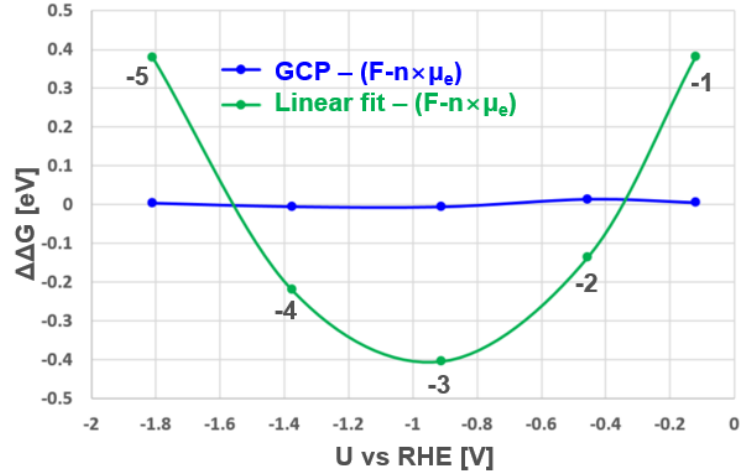


Fig. S1 Energy deviation from explicit calculations of the grand free energy (G) of 2CO^* on $\text{Cu}(111)$ surface as function of applied potential. The error compared to G for each method, GCP (blue) and linear fit (Green) are plotted at five different charges, Δn (net charge) = -1, -2, ..., -5, covering from -0.12 V_{RHE} to -1.81 V_{RHE} at pH 7.

While GCP correctly follows the G with about errors of 0.01 eV, the large quadratic deviation of linear fitting compared to the explicit calculation of G is clearly observed. This means that the errors mostly come from the absence of the capacitive property in the linear fitting method. The errors from the linear fit ranges from +0.4 eV \sim -0.4 eV depending on potential. The error of 0.4 eV can cause very large errors in estimating TOF ($\sim \times 10^6$ at room temperature).

Besides the GCP-K method providing accurate energetics, it also provides information about

- the capacitance of the electrode/electrolyte interface,
- the correct equilibrium number of electrons at any given potential (including the potential at 0 charge), and
- the evolution of all atomic configurations including the transition state as a function of applied potential

information not available from linear (or even simple quadratic) fitting.

The accuracy of the linear method could be improved by partitioning of each potential range with dense electron increment, but GCP-K does not require such corrections. Therefore, we consider that the use of capacitive term is very important.

Our GCP-K method is also valid to the transition state which allows how kinetic barrier and its atomic configuration evolve as function of potential. Fig. S2 shows the kinetic barrier and C-C bond distance at the transition state on $\text{Cu}^0/\text{Cu}_2\text{O}$ catalysts. The kinetic barrier gradually decreases as the electrode negatively polarizes while the C-C bond distance increase as potential decrease because the relatively greater stabilization for the final (FS, OCCO*) at large negative potential leading to the closer TS towards IS (2CO^*).

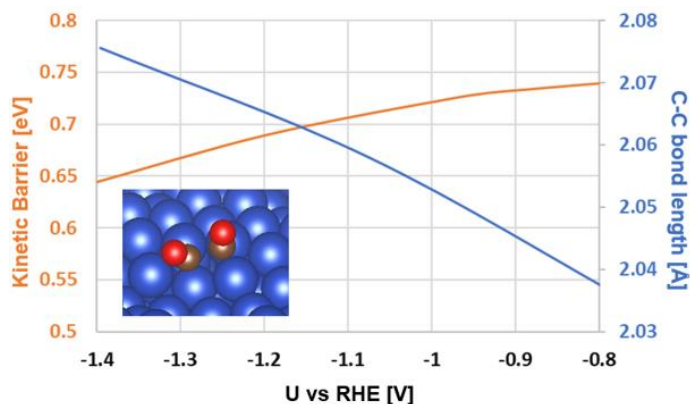


Fig. S2 The free energy kinetic barrier for CO dimerization on $\text{Cu}^0/\text{Cu}_2\text{O}$ catalyst as function of potential (orange) and the corresponding C-C bond length at the transition state (blue).

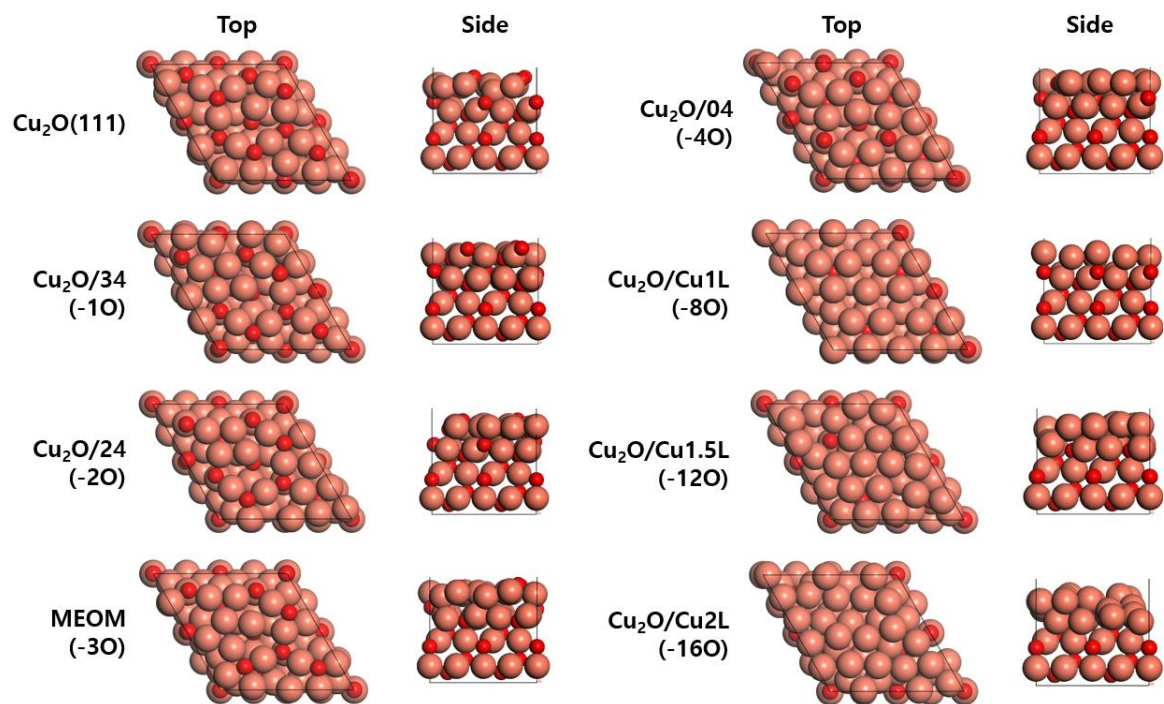


Fig. S3 Top and side views of various surface phases considered in surface free energy diagrams. Total numbers of oxygen on the top/bottom layers in the top tri-layer (O-Cu-O). The number of reduced oxygen also indicated in the parenthesis.

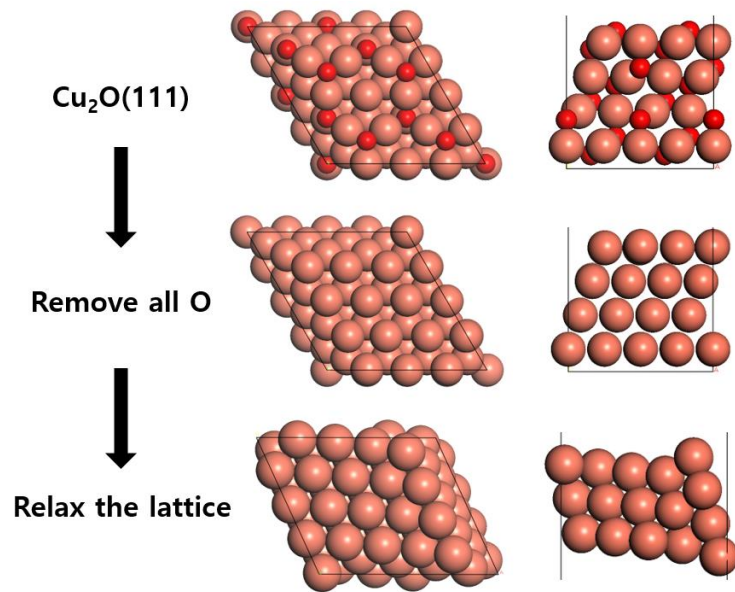


Fig. S4 Full relaxation after removing all oxygen from $\text{Cu}_2\text{O}(111)$. The final $\text{Cu(S)}[4(111) \times (111)]$ surface has (111) terrace with (111) step. We speculate that the step originates from the small size of supercell we used.

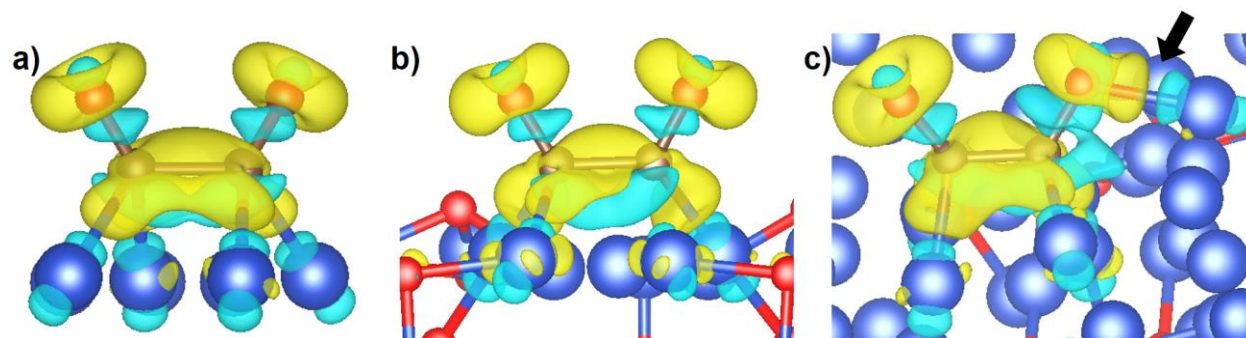


Fig. S5 Charge difference of (catalyst + OCCO*) – catalyst – OCCO* for (a) Cu111, (b) MEOM, and (c) Cu⁰/Cu₂O catalysts. The yellow indicates charge accumulation while and blue indicates depletion. Isosurface level of 0.005 a₀⁻³ (a₀: Bohr radius). In addition to typical charge donation and back donation interaction between Cu d orbital and the respective CO 5σ and 2π* orbitals, the further charge donation to intermediate occurs through (OCC)O-Cu bond.

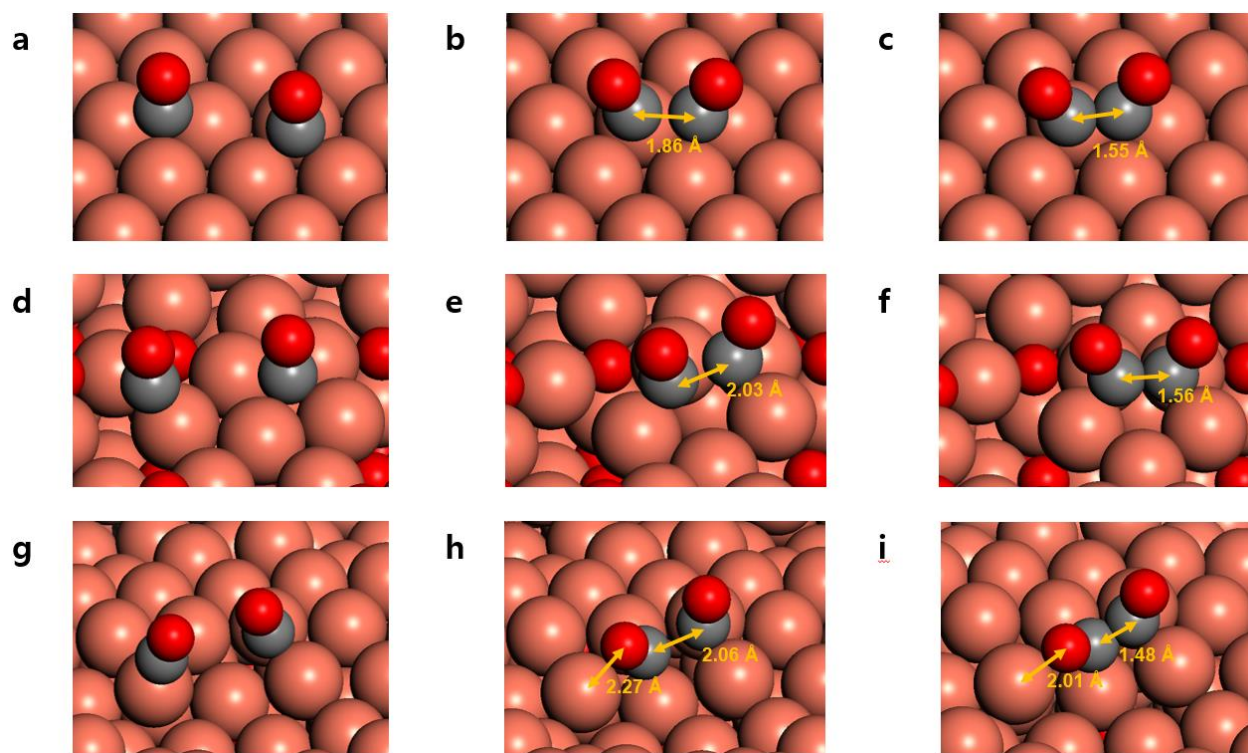


Fig. S6 The atomic configurations of CO dimerization reaction on (a-c) Cu(111), (d-f) MEOM and (g-i) Cu⁰/Cu₂O catalysts. (a, d, g), (b, e, h), and (c, f, i) corresponds to the initial (IS), transition (TS) and final states (FS), respectively. The C-C bond distances are indicated for all TS and FS and Cu-O bond distance is also indicated for Cu⁰/Cu₂O catalysts.

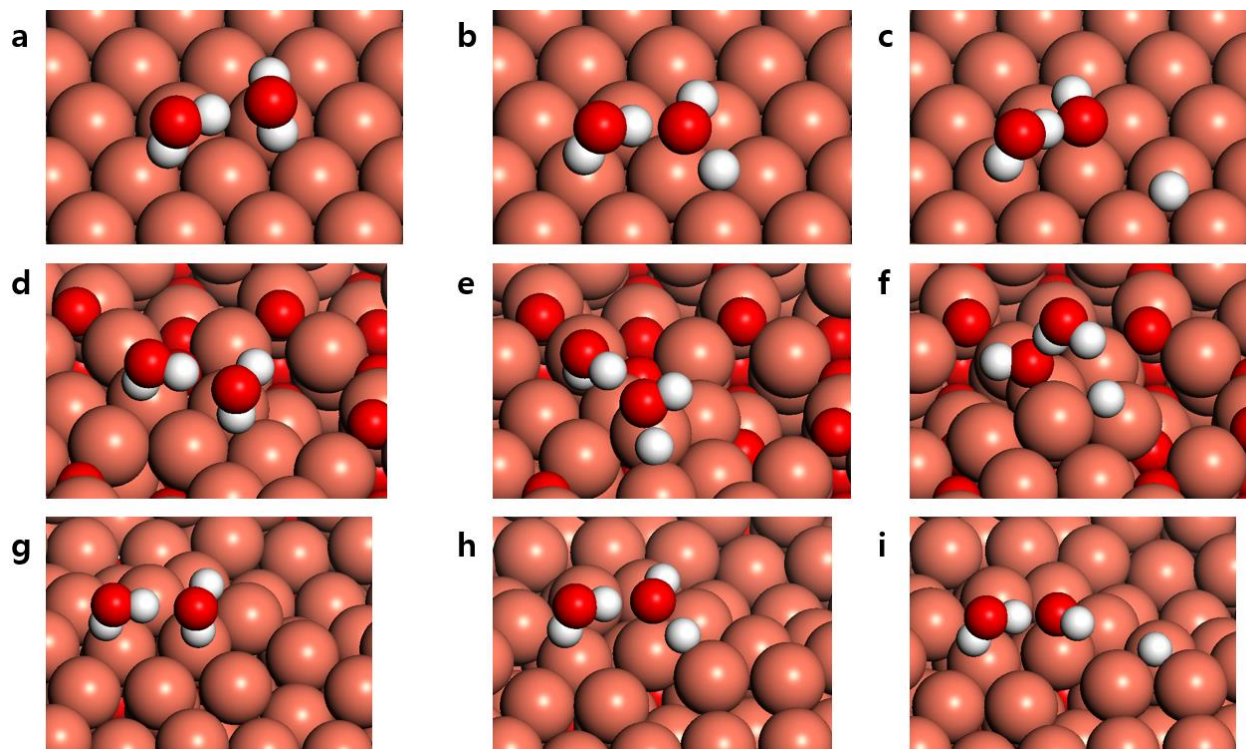


Fig. S7 The atomic configurations of Volmer reactions on (a-c) Cu(111), (d-f) MEOM and (g-i) Cu⁰/Cu₂O catalysts. (a, d, g), (b, e, h), and (c, f, i) corresponds to the initial (IS), transition (TS) and final states (FS), respectively.

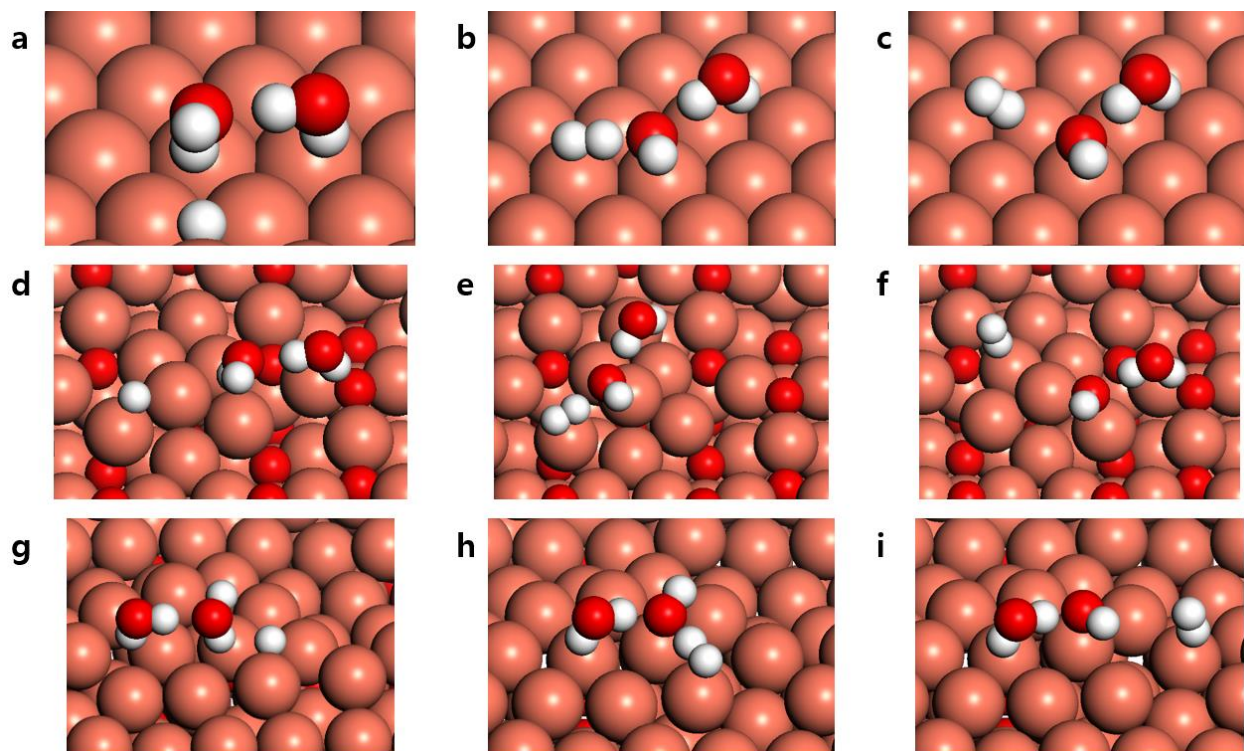


Fig. S8 The atomic configurations of Heyrovsky reactions on (a-c) Cu(111), (d-f) MEOM and (g-i) Cu⁰/Cu₂O catalysts. (a, d, g), (b, e, h), and (c, f, i) corresponds to the initial (IS), transition (TS) and final states (FS), respectively.

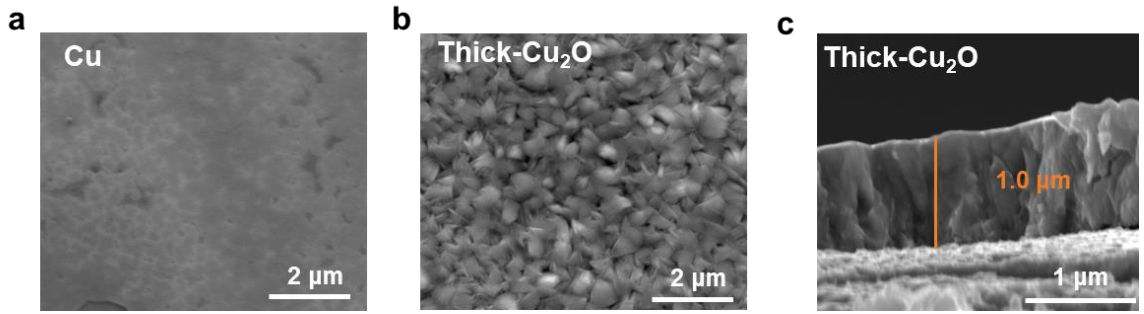


Fig. S9 SEM images of (a) as-prepared Cu; (b) as-prepared thick-Cu₂O; (c) Cross-section of as-prepared thick-Cu₂O.

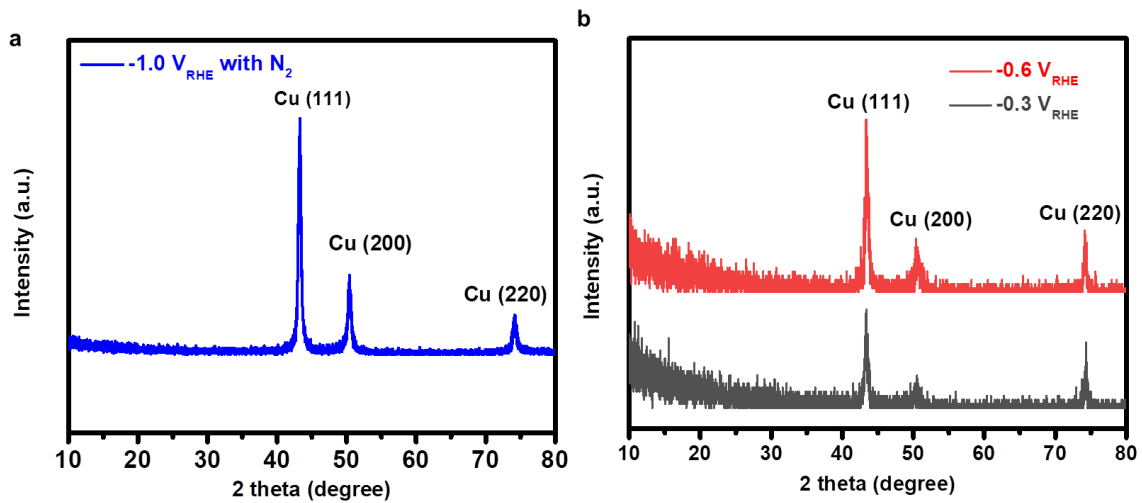


Fig. S10 *ex-situ* GIXRD analysis of thick- Cu_2O over 1h electrolysis (a) at $-1.0 V_{RHE}$ in N_2 -saturated $0.1 M KHCO_3$ electrolyte (pH 8); (b) at $-0.3 V_{RHE}$ and $-0.6 V_{RHE}$ in CO_2 -saturated $0.1 M K_2CO_3$ electrolyte (pH 7).

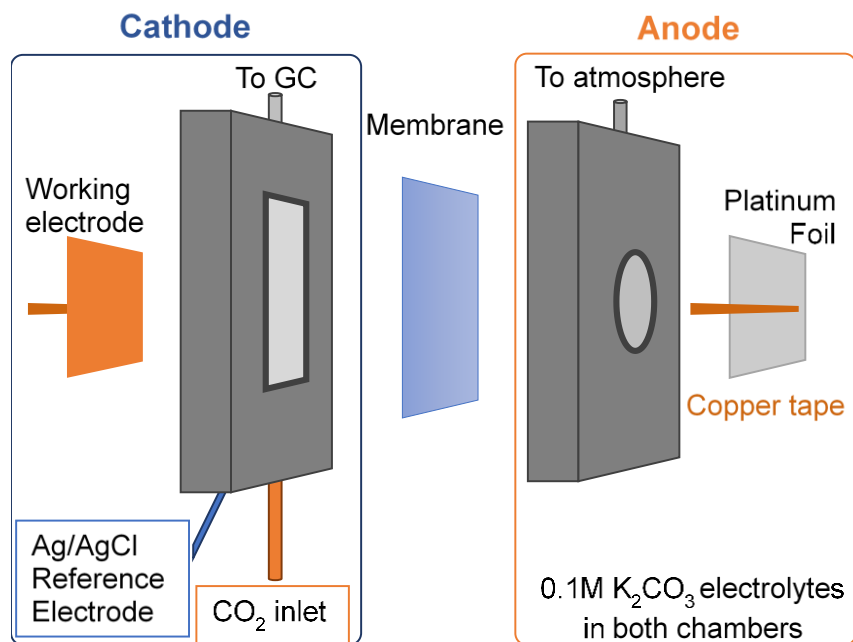


Fig. S11 Two-compartment flow cell used for bulk electrolysis of carbon dioxide.

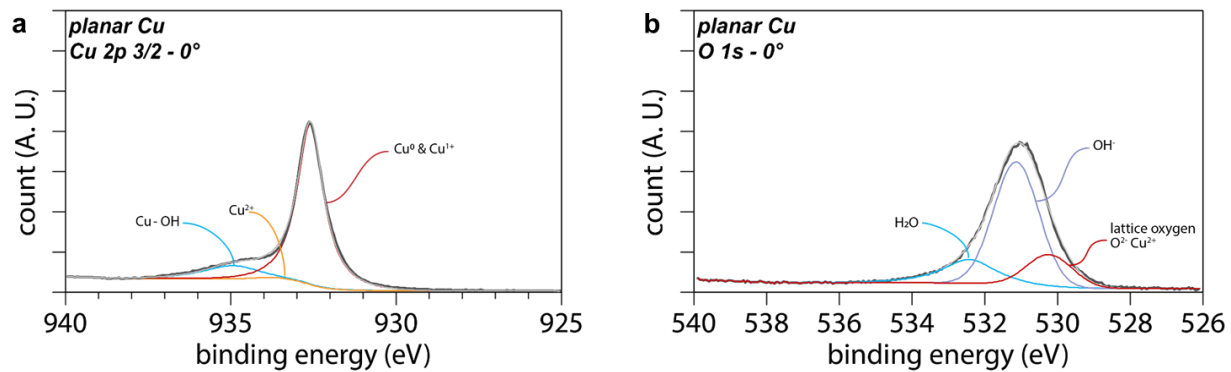


Fig. S12 XPS analysis on as-prepared Cu: (a) Cu_{2p} spectra of Cu; (b) O_{1s} spectra of Cu.

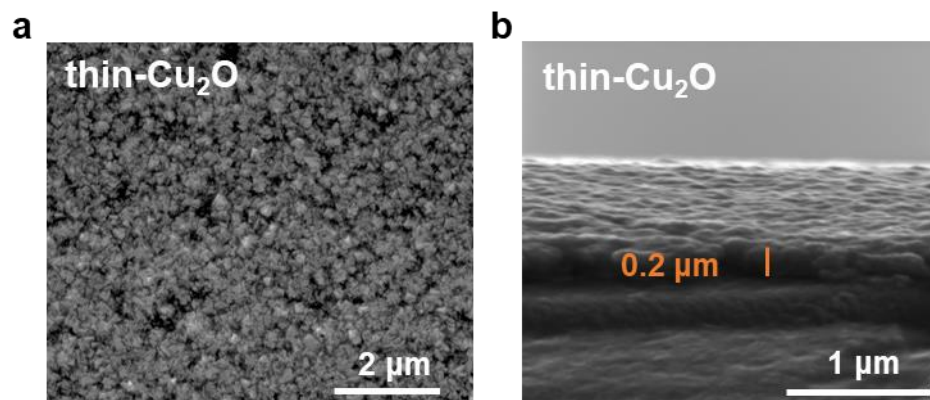


Fig. S13 SEM images of (a) thin-Cu₂O; (b) Cross-section of thin-Cu₂O.

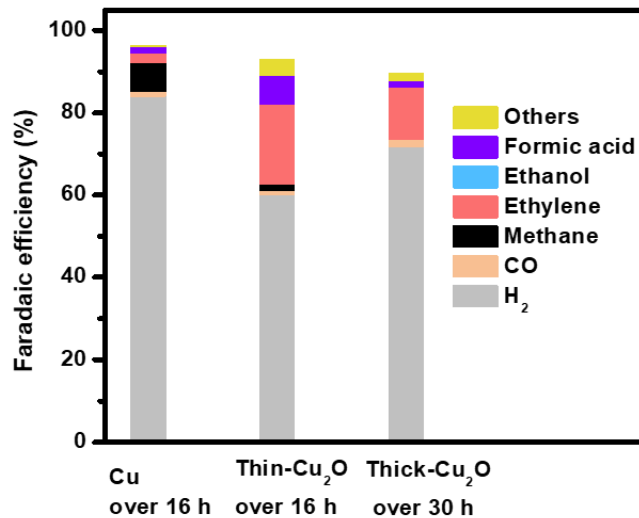


Fig. S14 Faradaic efficiencies of CO₂RR toward H₂ (grey), CO (gold), methane (black), ethylene (pink), ethanol (blue), formic acid (purple) and others: acetate, ethylene glycol and 1-propanol (yellow) for Cu over 16 h; thin-Cu₂O over 16 h; and thick-Cu₂O over 30 h at -1.0 V_{RHE} in CO₂-saturated 0.1 M K₂CO₃ electrolyte (pH 7).

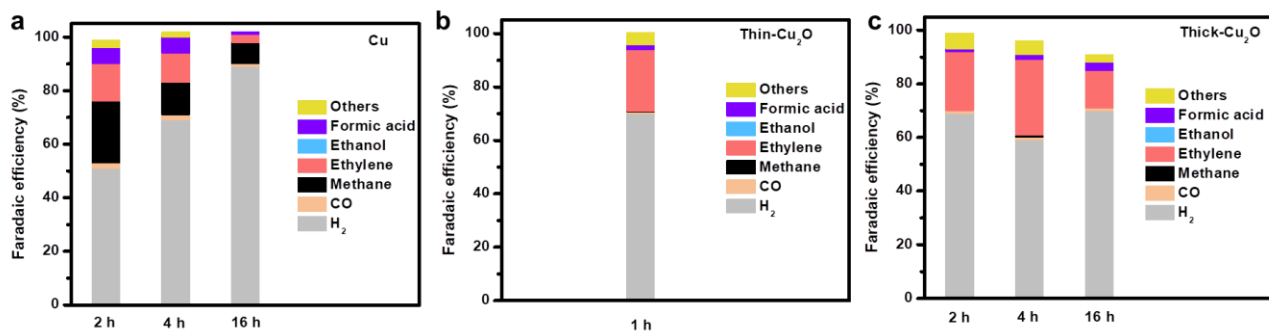


Fig. S15 Faradaic efficiencies of CO₂RR toward H₂ (grey), CO (gold), methane (black), ethylene (pink), ethanol (blue), formic acid (purple) and others: acetate, ethylene glycol and 1-propanol (yellow) for a Cu; b thin-Cu₂O; and c thick-Cu₂O at -1.0 V_{RHE} in CO₂-saturated 0.1 M K₂CO₃ electrolyte (pH 7). In the present study, we do not find a correlation for the production of ethanol on polycrystalline Cu, thin-Cu₂O, or thick-Cu₂O over time.

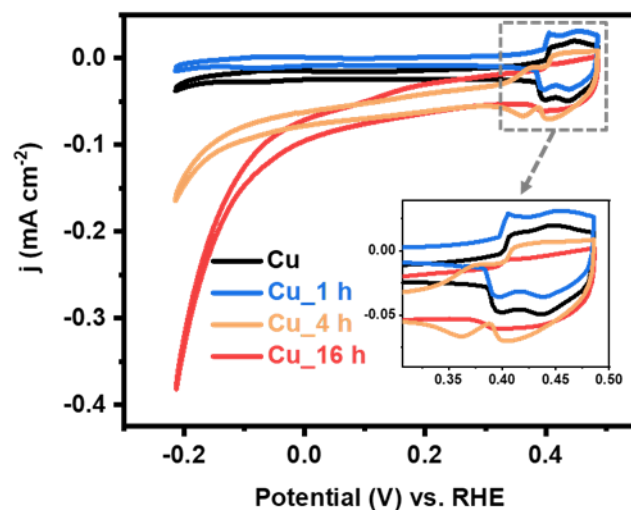


Fig. S16 CV profiles of pristine polycrystalline Cu and Cu after 16 h CO₂RR recorded in 0.1 M Ar saturated NaOH electrolyte at 50 mV s⁻¹, inset: enlarged region for 0.3-0.5 V. We have compared CV profiles on pristine polycrystalline Cu and Cu after 1, 4 and 16 h CO₂RR in 0.1 M NaOH.

The characteristic features in the CVs of Cu samples agree well with previous report(1) for polycrystalline Cu. According to previous report(1), the feature at -0.15 V can be assigned to OH adsorption/desorption on (100) terraces, while that at 0.06 V is related to OH adsorption/desorption on (111) sites. Our CV profiles indicate that the structures on pristine polycrystalline Cu and Cu after 1, 4, 16 h CO₂RR do not exhibit specific facet orientation. Therefore, we do not expect that surface texturing contributes in a significant way to alter C₂ selectivity on polycrystalline Cu over time.

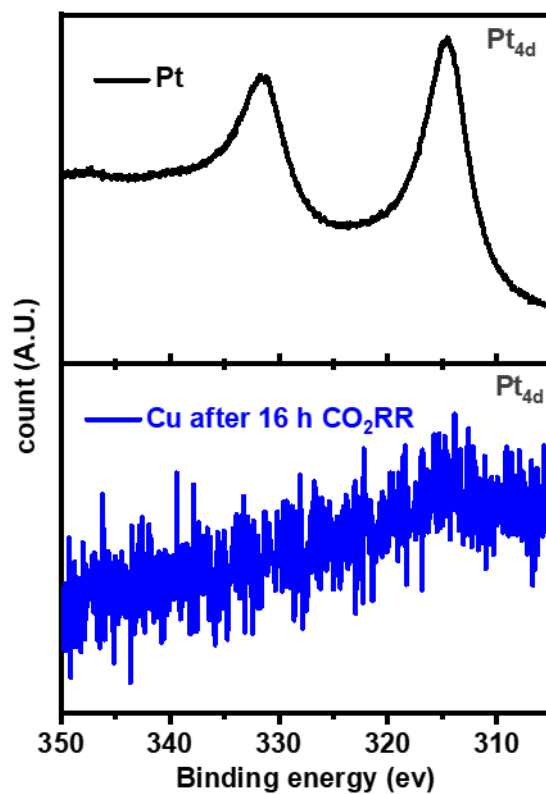


Fig. S17 Pt_{4d} spectra of Cu through long-term CO₂RR at -1.0 V_{RHE} in 0.1 M K₂CO₃ electrolyte (pH 7), a Pt foil was used as comparison. No contamination of Pt was found on Cu through long-term CO₂RR.

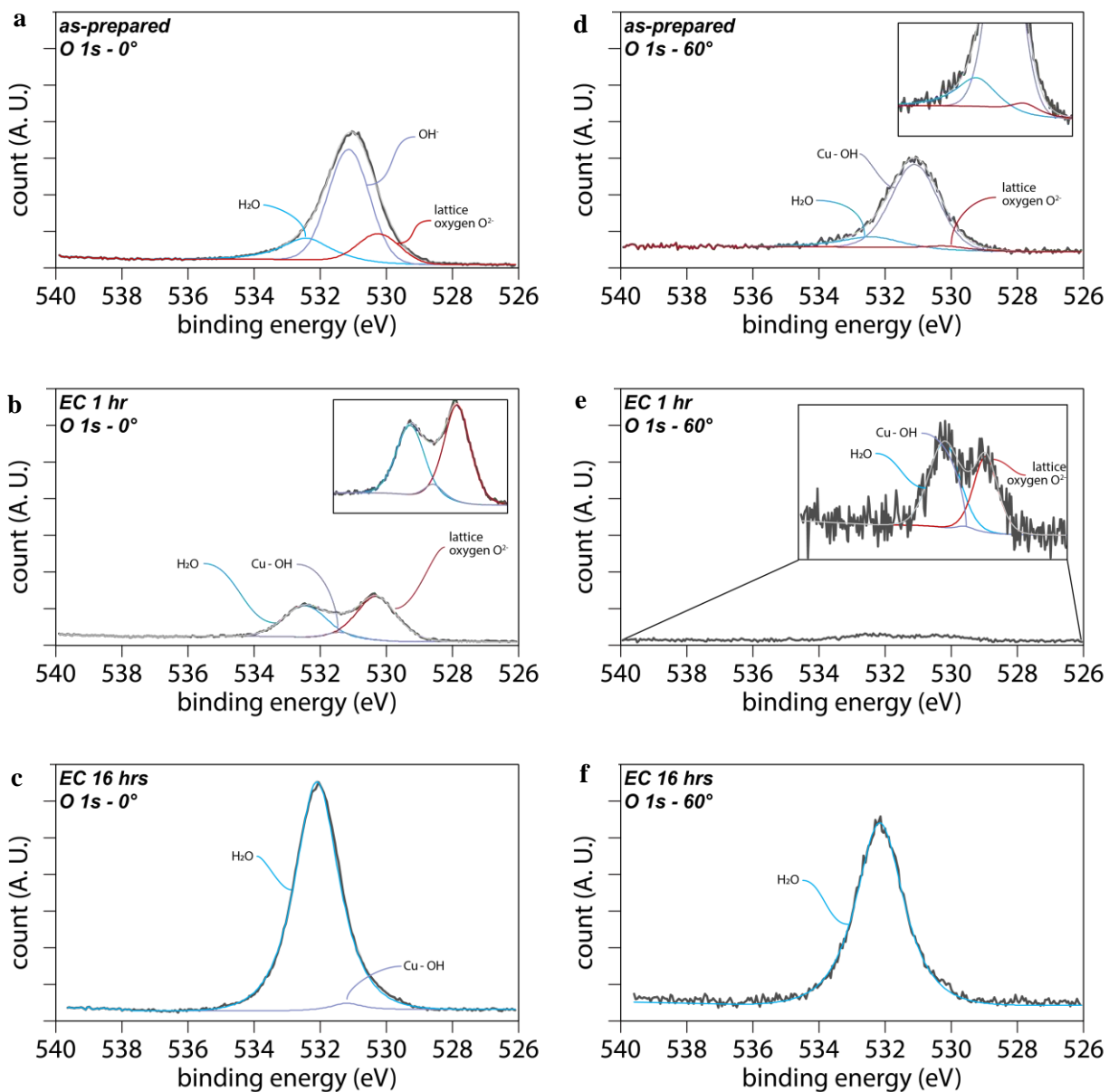


Fig. S18 AR-XPS analysis of O_{1s} spectra on Cu through long-term CO_2RR : (a) O_{1s} spectrum of as-prepared Cu at 0° ; (b) O_{1s} spectrum of Cu after 1h CO_2RR at 0° ; (c) O_{1s} spectrum of Cu after 16 h CO_2RR at 0° ; (d) O_{1s} spectrum of as-prepared Cu at 60° ; (e) O_{1s} spectrum of Cu after 1h CO_2RR at 60° ; (f) O_{1s} spectrum of Cu after 16 h CO_2RR at 60° ; Insets in each panel are enlarged to reveal the sub-peaks.

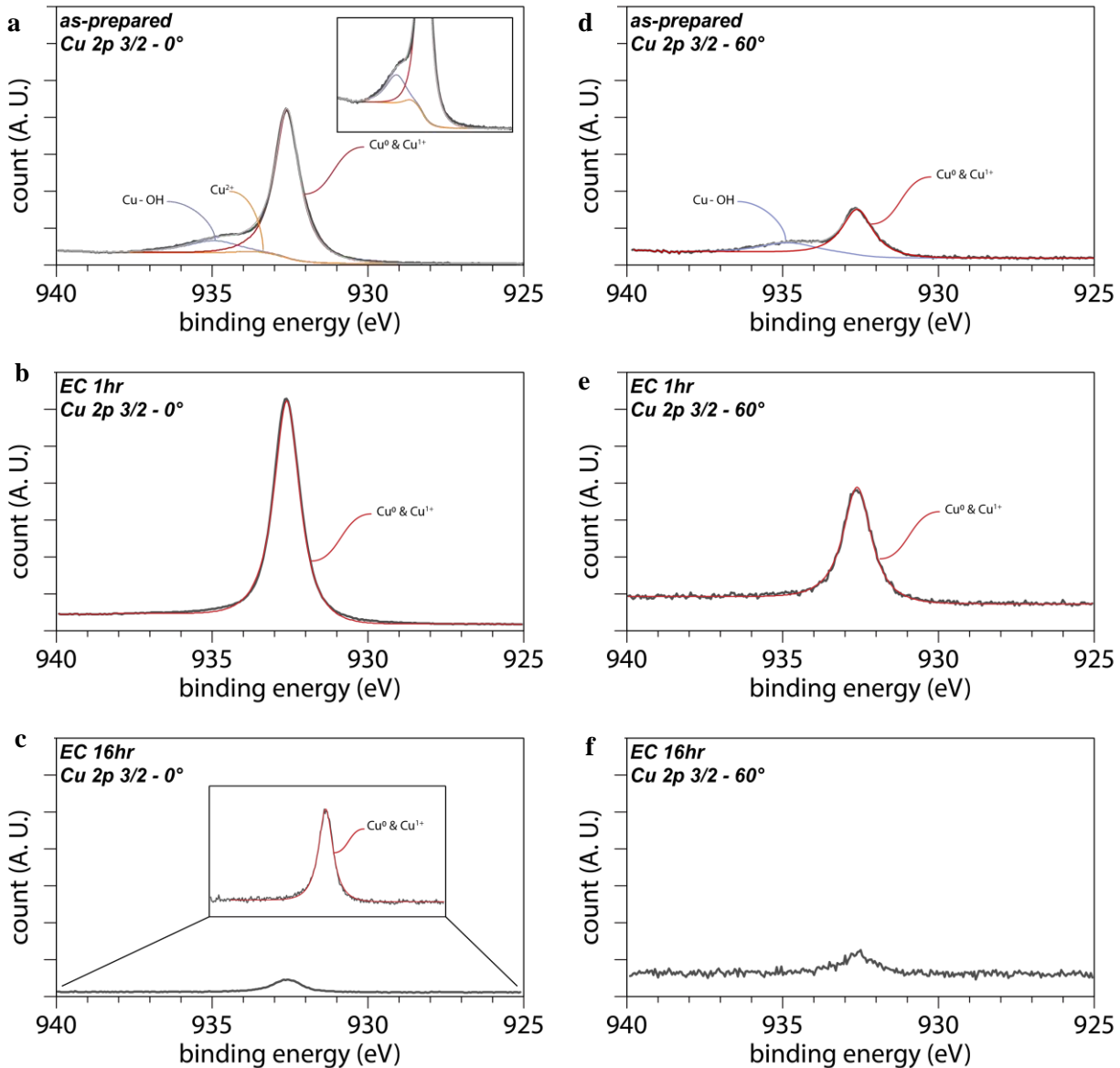


Fig. S19 AR-XPS analysis of Cu_{2p} spectra on Cu through long-term CO₂RR: (a) Cu_{2p} spectrum of as-prepared Cu at 0°; (b) Cu_{2p} spectrum of Cu after 1h CO₂RR at 0°; (c) Cu_{2p} spectrum of Cu after 16 h CO₂RR at 0°; (d) Cu_{2p} spectrum of as-prepared Cu at 60°; (e) Cu_{2p} spectrum of Cu after 1h CO₂RR at 60°; (f) Cu_{2p} spectrum of Cu after 16 h CO₂RR at 60°; Insets in each panel are enlarged to reveal the sub-peaks.

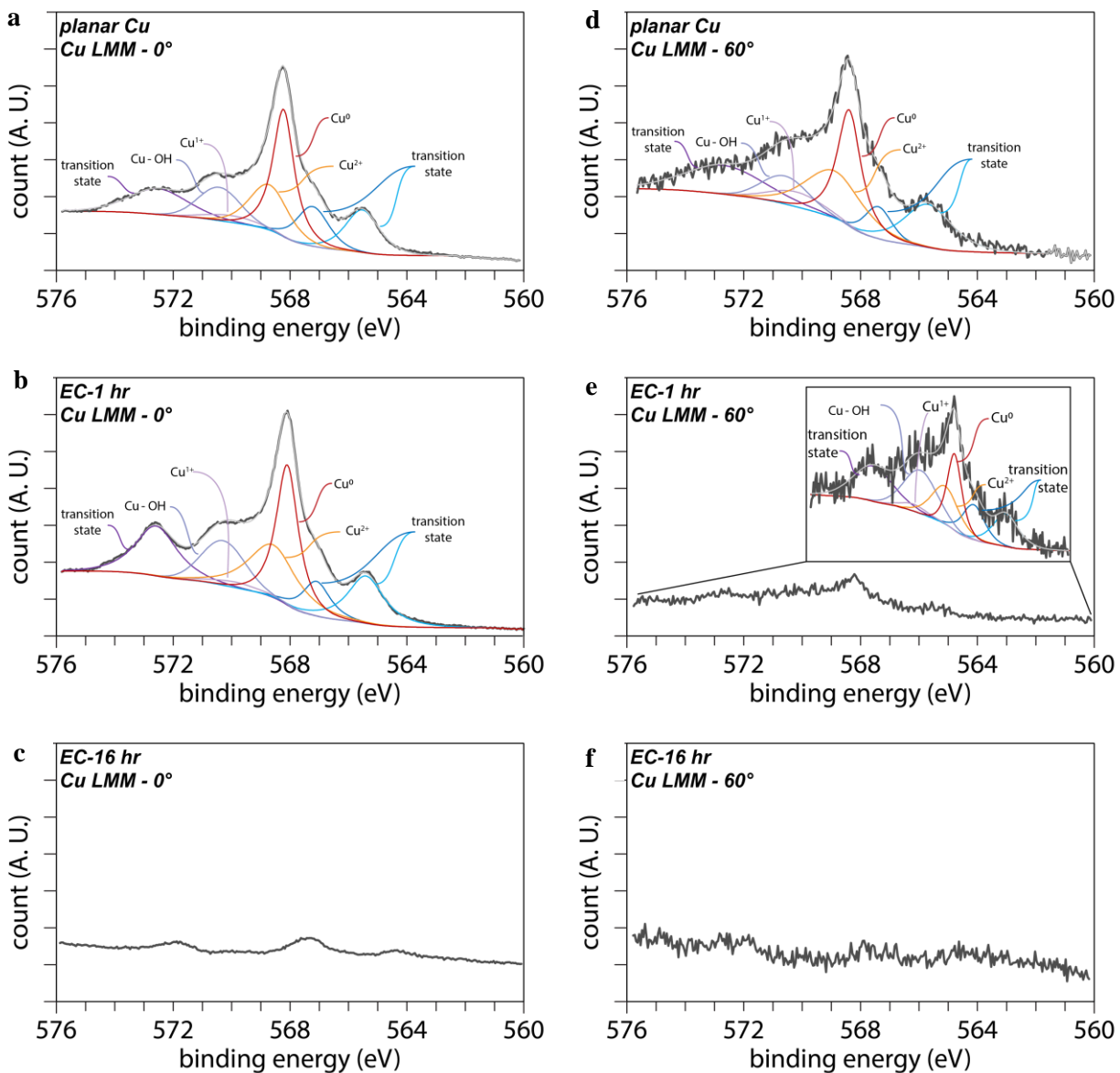


Fig. S20 AR-XPS analysis of Cu LMM spectra on Cu through long-term CO₂RR: (a) Cu LMM spectrum of as-prepared Cu at 0°; (b) Cu LMM spectrum of Cu after 1h CO₂RR at 0°; (c) Cu LMM spectrum of Cu after 16 h CO₂RR at 0°; (d) Cu LMM spectrum of as-prepared Cu at 60°; (e) Cu LMM spectrum of Cu after 1h CO₂RR at 60°; (f) Cu LMM spectrum of Cu after 16 h CO₂RR at 60°; Insets in each panel are enlarged to reveal the sub-peaks.

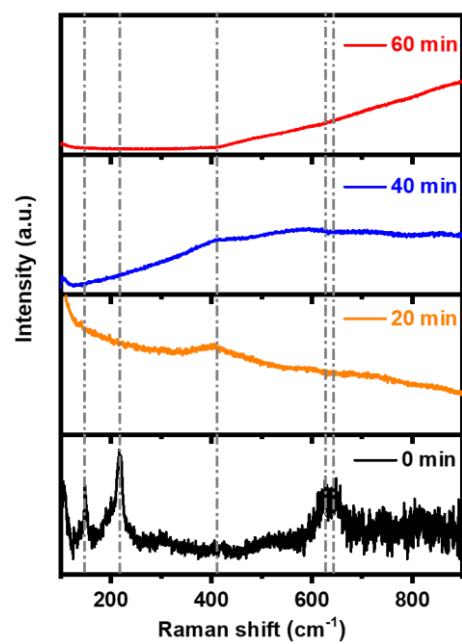


Fig. S21 *In-situ* Raman spectra of thick-Cu₂O in 0.1 M K₂CO₃ (CO₂ saturated) electrolyte at -1.0 V_{RHE} over time. Characteristic features of Cu₂O totally disappeared within 1 h, while Raman peaks for adsorbed *CO (282 and 355–366 cm⁻¹) are not observed.

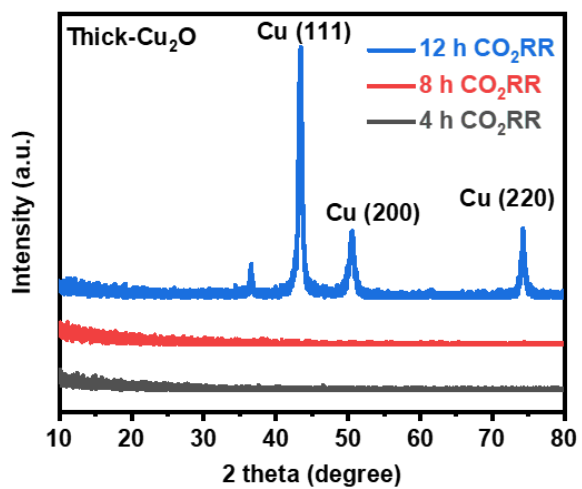


Fig. S22 *Ex-situ* GIXRD analysis of thick-Cu₂O over CO₂RR at -1.0 V_{RHE} in CO₂-saturated 0.1 M K₂CO₃ electrolyte (pH 7).

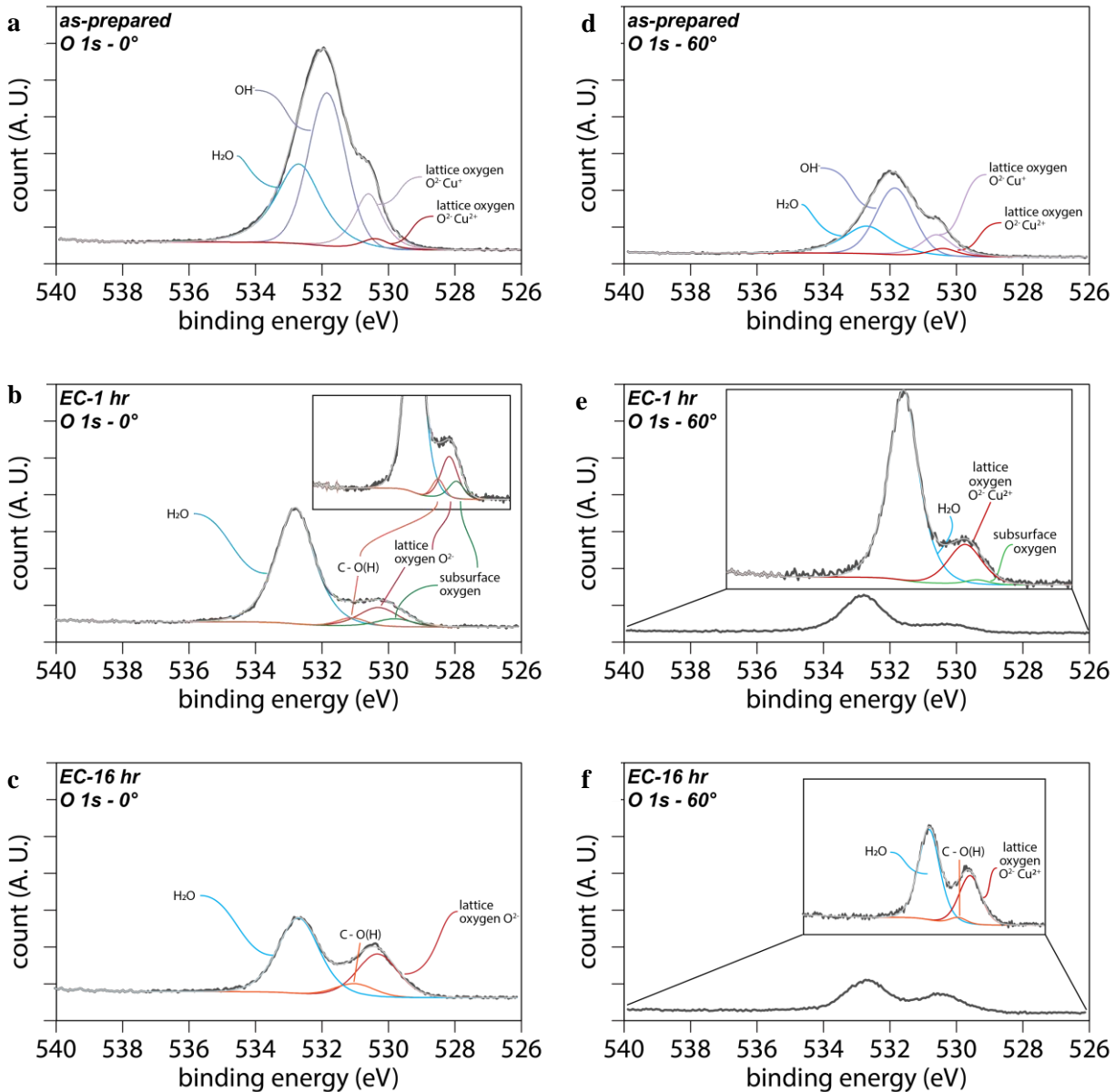


Fig. S23 AR-XPS analysis of O_{1s} spectra on thick- Cu_2O through long-term CO_2RR : (a) O_{1s} spectrum of as-prepared thick- Cu_2O at 0° ; (b) O_{1s} spectrum of thick- Cu_2O after 1h CO_2RR at 0° ; (c) O_{1s} spectrum of thick- Cu_2O after 16 h CO_2RR at 0° ; (d) O_{1s} spectrum of as-prepared thick- Cu_2O at 60° ; (e) O_{1s} spectrum of thick- Cu_2O after 1h CO_2RR at 60° ; (f) O_{1s} spectrum of Cu after 16 h CO_2RR at 60° . The observed oxygen was deconvoluted into lattice oxygen presumably due to re-oxidation and subsurface oxygen based on literature reports(2, 3). As thick- Cu_2O after 16 h CO_2RR mostly produced H_2 (Fig. 4F), the residue subsurface oxygen in the lattice should be almost gone. Indeed, we observed only re-oxidized lattice oxygen of thick- Cu_2O after 16 h CO_2RR , while subsurface oxygen was absent; Insets in each panel are enlarged to reveal the sub-peaks.

Cu₂O			-10			-20			MEOM (-30)		
F(n)	n	mu	F(n)	n	mu	F(n)	n	mu	F(n)	n	mu
-13432.21506	1408	-0.14296	-13416.11743	1402	-0.15453	-13400.00752	1396	-0.15436	-13383.95043	1390	-0.1587
-13432.36341	1409	-0.14296	-13416.26613	1403	-0.14448	-13400.15734	1397	-0.14499	-13384.10495	1391	-0.14908
-13432.50228	1410	-0.1326	-13416.40748	1404	-0.13538	-13400.29849	1398	-0.13669	-13384.25007	1392	-0.13965
-13432.62778	1411	-0.11769	-13416.53726	1405	-0.12169	-13400.42933	1399	-0.1237	-13384.38229	1393	-0.12477
-13432.7387	1412	-0.10402	-13416.65274	1406	-0.1082	-13400.54616	1400	-0.10993	-13384.49954	1394	-0.10979
-13432.83655	1413	-0.10402	-13416.75597	1407	-0.09602	-13400.65035	1401	-0.09762	-13384.62088	1395	-0.10017

-40			-80			-120			Cu⁰/Cu₂O (-160)		
F(n)	n	mu	F(n)	n	mu	F(n)	n	mu	F(n)	n	mu
-13367.75442	1384	-0.15408	-13303.2219	1360	-0.15309	-13239.00094	1336	-0.15459	-13174.7388	1312	-0.15367
-13367.90319	1385	-0.14451	-13303.37003	1361	-0.14474	-13239.15116	1337	-0.14657	-13174.88743	1313	-0.1457
-13368.04473	1386	-0.13847	-13303.51278	1362	-0.13919	-13239.29537	1338	-0.14079	-13175.03112	1314	-0.14052
-13368.17764	1387	-0.12651	-13303.64706	1363	-0.12845	-13239.43248	1339	-0.13018	-13175.16648	1315	-0.12949
-13368.29769	1388	-0.11364	-13303.76959	1364	-0.11632	-13239.55642	1340	-0.11772	-13175.28965	1316	-0.11691
-13368.40499	1389	-0.10126	-13303.88063	1365	-0.10466	-13239.66859	1341	-0.10581	-13175.40041	1317	-0.10489

Table S1 Total energy (F), number of electrons (n), electrochemical potential (mu) for all eight states considered in surface Pourbaix diagram.

MEOM

CO dimerization

IS			TS			FS		
F(n)	n	mu	F(n)	n	mu	F(n)	n	mu
-13427.83973	1412	-0.13909	-13427.81051	1412	-0.14228	-13427.83317	1412	-0.14637
-13427.97097	1413	-0.12326	-13427.94472	1413	-0.12576	-13427.97158	1413	-0.12979
-13428.08664	1414	-0.10819	-13428.06252	1414	-0.11003	-13428.0931	1414	-0.11393

Volmer

IS			TS			FS		
F(n)	n	mu	F(n)	n	mu	F(n)	n	mu
-13418.83418	1408	-0.14015	-13418.81216	1408	-0.14476	-13418.84477	1408	-0.14193
-13418.96592	1409	-0.12345	-13418.95335	1409	-0.13082	-13418.97923	1409	-0.12686
-13419.08156	1410	-0.10887	-13419.08042	1410	-0.11764	-13419.0988	1410	-0.11237

Heyrovsky

IS			TS			FS		
F(n)	n	mu	F(n)	n	mu	F(n)	n	mu
-13419.45757	1409	-0.14178	-13419.42239	1409	-0.14127	-13419.44713	1409	-0.13915
-13419.59296	1410	-0.12728	-13419.55606	1410	-0.12615	-13419.57985	1410	-0.12554
-13419.71299	1411	-0.11308	-13419.6754	1411	-0.11295	-13419.69918	1411	-0.1133

Cu⁰/Cu₂O

CO dimerization

IS			TS			FS		
F(n)	n	mu	F(n)	n	mu	F(n)	n	mu
-13218.74903	1335	-0.12687	-13218.72147	1335	-0.12879	-13218.74827	1335	-0.1303
-13218.86999	1336	-0.11472	-13218.84385	1336	-0.11665	-13218.87234	1336	-0.11849
-13218.97714	1337	-0.10341	-13218.95389	1337	-0.10477	-13218.98454	1337	-0.10662

Volmer

IS	TS	FS
----	----	----

F(n)	n	mu	F(n)	n	mu	F(n)	n	mu
-13209.61	1330	-0.13851	-13209.57892	1330	-0.13915	-13209.61369	1330	-0.14139
-13209.7438	1331	-0.12876	-13209.71332	1331	-0.12959	-13209.7499	1331	-0.13037
-13209.86704	1332	-0.11768	-13209.83361	1332	-0.11863	-13209.87409	1332	-0.11877

Heyrovsky

IS			TS			FS		
F(n)	n	mu	F(n)	n	mu	F(n)	n	mu
-13210.20573	1331	-0.13851	-13210.18543	1331	-0.13861	-13210.18451	1331	-0.13984
-13210.33923	1332	-0.12835	-13210.31921	1332	-0.12867	-13210.3195	1332	-0.12948
-13210.46185	1333	-0.11698	-13210.44218	1333	-0.11757	-13210.44372	1333	-0.11892

Cu(111)

CO dimerization

IS			TS			FS		
F(n)	n	mu	F(n)	n	mu	F(n)	n	mu
-12962.10315	1238	-0.1391	-12962.06353	1238	-0.14341	-12962.0623	1238	-0.14069
-12962.23435	1239	-0.12245	-12962.19937	1239	-0.126	-12962.19991	1239	-0.12645
-12962.34825	1240	-0.10546	-12962.31237	1240	-0.10743	-12962.31941	1240	-0.11012

Volmer

IS			TS			FS		
F(n)	n	mu	F(n)	n	mu	F(n)	n	mu
-12953.10715	1234	-0.13957	-12953.06883	1234	-0.14176	-12953.09661	1234	-0.14249
-12953.23919	1235	-0.1236	-12953.20295	1235	-0.12565	-12953.23128	1235	-0.12586
-12953.35446	1236	-0.10693	-12953.32358	1236	-0.1106	-12953.34859	1236	-0.10872

Heyrovsky

IS			TS			FS		
F(n)	n	mu	F(n)	n	mu	F(n)	n	mu
-12953.69694	1235	-0.13914	-12953.6652	1235	-0.13916	-12953.6677	1235	-0.14117
-12953.82861	1236	-0.1234	-12953.79622	1236	-0.12325	-12953.80217	1236	-0.12735
-12953.94385	1237	-0.10725	-12953.91057	1237	-0.10644	-12953.92295	1237	-0.1143

Table S2 Total energy (F), number of electrons (n), electrochemical potential (μ) for all elementary reactions considered in this study.

A	Cu	H ₂	CO	Methane	Formic Acid	Ethylene	Ethanol	Others	Total FE	Total Current (mA/cm ²)
	Average	46%	5%	10%	14%	17%	6%	1%	99%	2.73
	SEM	6%	1%	2%	2%	4%	3%	0%	3%	0.09
	STD	10%	1%	3%	4%	6%	5%	0%	5%	0.15
	<i>Trial 1</i>	41%	4%	9%	9%	22%	8%	1%	94%	2.90
	<i>Trial 2</i>	57%	5%	8%	16%	10%	0%	1%	98%	2.64
	<i>Trial 3</i>	40%	6%	14%	16%	18%	10%	1%	105%	2.64

B	Cu ₂ O	H ₂	CO	Methane	Formic Acid	Ethylene	Ethanol	Others	Total FE	Total Current (mA/cm ²)
	Average	39%	1%	0%	6%	35%	10%	2%	95%	1.61
	SEM	3%	0%	0%	1%	2%	1%	0%	1%	0.07
	STD	5%	0%	0%	1%	3%	2%	0%	3%	0.11
	<i>Trial 1</i>	36%	1%	1%	7%	37%	11%	2%	94%	1.58
	<i>Trial 2</i>	45%	1%	0%	5%	31%	12%	2%	97%	1.73
	<i>Trial 3</i>	37%	1%	1%	7%	36%	9%	2%	92%	1.51

Table S3 Faradaic efficiencies of CO₂RR and total current for (A) Cu and (B) Cu₂O, reported in Fig. 2e.

Sample	Be (ppb)	Al (ppb)	V (ppb)	Mn (ppb)	Fe (ppb)	Co (ppb)	Ni (ppb)	Ag (ppb)	Cd (ppb)	In (ppb)	Sn (ppb)	Au (ppb)	Pt (ppb)
Pristine K ₂ CO ₃	0.0	0.0	0.0	0.0	0.0	0.0	0.0	1.5	0.0	0.0	0.5	0.0	0.1
K ₂ CO ₃ _1 h CO ₂ RR	0.0	0.0	0.0	0.0	0.0	0.0	0.0	0.0	0.0	0.0	0.3	0.0	0.5
K ₂ CO ₃ _4 h CO ₂ RR	0.0	0.0	0.0	0.0	0.0	0.0	0.0	0.0	0.0	0.0	0.1	0.0	0.4

Table S4 Metal ions in the pristine K₂CO₃ electrolyte, K₂CO₃ electrolytes through 1 h and 4 h CO₂RR on polycrystalline Cu, respectively, detected by ICP-MS. The pristine K₂CO₃ electrolyte shows trace amount of metal ions such as Ag, Sn and Pt. The amount of metal ions in the electrolytes after 1 h and 4 h CO₂RR are comparable, remaining within trace level. Therefore, the selectivity switch from ethylene to H₂ on Cu over the first 4 h is unlikely due to the progressive contamination from metal ions in the electrolyte.

Angle (°) \ Testing time (h)	0	60
0	0.882	4.207
1	0.737	1.304
16	N/A	N/A

Table S5 Ratio between adsorbed H₂O and lattice oxygen (H₂O/O²⁻) for pristine planar copper and copper tested for 1 hour and 16 hours in Fig. S18. We can see that with increasing of the incident angle, the ratio between water and lattice oxygen increases as well, which indicates the presence of subsurface oxygen, while the adsorbed water molecules are only at the topmost surface.

Oxygen species	0 hour (Left: 0°, Right: 60°)		1 hour (Left: 0°, Right: 60°)		16 hours (Left: 0°, Right: 60°)	
	Lattice oxygen	1.983	1.301	6.306	4.53	1.816
Subsurface oxygen	N/A	N/A	16.254	58.898	N/A	N/A

Table S6 Ratio between adsorbed H₂O and lattice oxygen or adsorbed H₂O and subsurface oxygen for pristine thick-Cu₂O and thick-Cu₂O tested for 1 hour and 16 hours in Fig. S23. The water to subsurface oxygen ratio increases from 16.254 to 58.898, when the angle is increased to 60°, which supports that the assigned subsurface oxygen species are indeed underneath the topmost surface. However, the water to

lattice oxygen ratio does not significantly change with increasing of the incident beam angle, implying that both lattice oxygen (presumably due to re-oxidation) and water species are at the topmost surface.

References

1. Arán-Ais RM, Scholten F, Kunze S, Rizo R, & Roldan Cuenya B (2020) The role of in situ generated morphological motifs and Cu(i) species in C₂₊ product selectivity during CO₂ pulsed electroreduction. *Nature Energy* 5(4):317-325.
2. Bluhm H, *et al.* (2004) Methanol Oxidation on a Copper Catalyst Investigated Using in Situ X-ray Photoelectron Spectroscopy. *The Journal of Physical Chemistry B* 108(38):14340-14347.
3. Favaro M, *et al.* (2017) Subsurface oxide plays a critical role in CO₂ activation by Cu(111) surfaces to form chemisorbed CO₂, the first step in reduction of CO₂. *Proceedings of the National Academy of Sciences* 114(26):6706-6711.